Article

Investigating the Performance and Stability of Fe₃O₄/Bi₂MoO₆/g-C₃N₄ Magnetic Photocatalysts for the Photodegradation of Sulfonamide Antibiotics under Visible Light Irradiation

Ke Li [1,2], Miaomiao Chen [1], Lei Chen [1,*], Wencong Xue [1], Wenbo Pan [1] and Yanchao Han [2]

[1] Key Laboratory of Song Liao Aquatic Environment, Ministry of Education, Jilin Jianzhu University, Changchun 130118, China; like123@163.com (K.L.); chenm192@163.com (M.C.); xuewencong116@163.com (W.X.); panwenbo2023@163.com (W.P.)

[2] State Key Laboratory of Electroanalytical Chemistry, Changchun Institute of Applied Chemistry, Chinese Academy of Sciences, Changchun 130022, China; hyc@ciac.ac.cn

* Correspondence: chenlei.jliae@hotmail.com

Abstract: In this study, an Fe₃O₄/Bi₂MoO₆/g-C₃N₄ magnetic composite photocatalyst was synthesized for the visible-light-driven photocatalytic degradation of sulfonamide antibiotics, specifically sulfamerazine (SM1). Characterization techniques, including X-ray diffraction (XRD), scanning electron microscopy (SEM), X-ray photoelectron spectroscopy (XPS), Fourier transform infrared spectroscopy (FT-IR), photoluminescence spectroscopy (PL), UV-vis diffuse reflectance spectra (UV-vis), and the use of a vibrating sample magnetometer (VSM), were employed to analyze the fabricated samples. The composite exhibited efficient visible-light absorption and charge separation, with optimal photocatalytic performance achieved at a pH value of 9.0. The study reveals the importance of solution pH in the degradation process and the potential applicability of the composite for efficient magnetic separation and recycling in photocatalytic processes. The Fe₃O₄/Bi₂MoO₆/g-C₃N₄ magnetic composite photocatalyst demonstrated exceptional stability and recyclability, maintaining a high degradation efficiency of over 87% after five consecutive cycles. An XRD analysis conducted after the cycling tests confirmed that the composite's composition and chemical structure remained unchanged, further supporting its chemical stability. This investigation offers valuable insights into the photocatalytic degradation of sulfonamide antibiotics using magnetic composite photocatalysts and highlights the potential of the Fe₃O₄/Bi₂MoO₆/g-C₃N₄ composite for practical applications in environmental remediation.

Keywords: sulfonamide antibiotics; magnetic photocatalyst; Carbon nitride

1. Introduction

The presence of emerging contaminants, such as pharmaceuticals and personal care products (PPCPs), in the aquatic environment has raised increasing concern in recent years owing to their potential impact on ecosystems and human health [1–5]. As PPCPs, sulfonamide antibiotics have been extensively employed in both human and veterinary medicine worldwide [6–8]. Nevertheless, their improper disposal into wastewater systems results in their accumulation in aquatic ecosystems, leading to significant environmental and public health concerns [9–11]. Traditional techniques, such as membrane filtration [12], biodegradation [13], and adsorption [14], have been employed to address this issue. However, these conventional methods face challenges in effectively eradicating sulfonamide antibiotics from wastewater due to their high stability and resistance to biological treatment [15,16]. Therefore, there is an urgent need to develop innovative and efficient approaches to removing them.

Photocatalysis, as a promising advanced oxidation process (AOP), has emerged as a promising approach for the degradation of organic pollutants owing to its environmentally friendly nature, high level of efficiency, and potential for utilizing solar energy [17–19]. Among the numerous photocatalytic materials, graphitic carbon nitride (g-C$_3$N$_4$ or g-CN) has emerged as a metal-free, non-toxic, and environmentally friendly photocatalyst with a suitable bandgap for visible light absorption [20,21]. Despite its potential, the photocatalytic effectiveness of g-CN is hindered by several drawbacks: it suffers from a high rate of charge carrier recombination, a limited absorption spectrum in the visible light range, and lackluster electrical conductivity [22,23]. To overcome these limitations, various strategies have been explored, including heterojunction construction, metal or non-metal doping, defect engineering, and morphological control [24–29]. Heterostructure photocatalysts have the potential to reduce electron–hole recombination and bolster light absorption [30,31]. Therefore, the construction of a heterojunction between g-C$_3$N$_4$ and other semiconductors with well-matched band structures using a Z-scheme mechanism can significantly enhance the separation efficiencies of photogenerated charge carriers [32–34].

In recent years, bismuth-based semiconductors have garnered considerable attention owing to their remarkable visible light absorption capabilities and distinct electronic properties. Among these semiconductors, bismuth molybdate (Bi$_2$MoO$_6$) has emerged as a highly promising photocatalyst due to its exceptional photocatalytic performance, non-toxic nature, and chemical stability [35,36]. Bi$_2$MoO$_6$, with its unique layered structure and strong oxidizing potential, demonstrates advantageous properties that contribute to its effectiveness as a photocatalyst [37]. The Bi$_2$MoO$_6$ crystal structure comprises alternating MoO4 and Bi2O2 layers, resulting in a highly polarized lattice that promotes the generation of an internal electric field. This field serves to suppress the recombination of photogenerated charge carriers, thereby boosting the photocatalytic activity of the material [38]. The integration of graphitic carbon nitride (g-CN) with Bi$_2$MoO$_6$ forms a heterojunction that can substantially enhance charge carrier separation, leading to an improvement in the photocatalytic performance of the composite material [38,39]. The coupling of g-CN and Bi$_2$MoO$_6$ also facilitates the construction of Z-scheme systems, which have proven to be highly effective for various water remediation applications [40,41]. This heterojunction not only benefits from the synergistic effects of g-CN's appealing electronic structure and responsiveness to visible light but also capitalizes on Bi$_2$MoO$_6$'s excellent photocatalytic properties and chemical stability [40,42]. Addressing the challenge of conveniently and economically retrieving catalysts from a substantial volume of water without resulting in loss or clumping is paramount. Conventional retrieval methods, such as filtration and centrifugation, despite their effectiveness, are deemed time-consuming and costly and are thus not optimal for large-scale industrial implementations. The employment of nano-magnetite (Fe$_3$O$_4$), known for its superior superparamagnetic characteristics, has been explored to solve these retrieval issues by enabling the magnetic recovery of nanocomposites [43,44]. Fe$_3$O$_4$ nanoparticles offer the benefits of enhancing photocatalytic performance due to their exceptional electrical conductivity, high surface-to-volume ratios, and notable optical and chemical attributes [45,46]. Additionally, Fe$_3$O$_4$ facilitates charge separation when integrated with other nanocomposites as it traps photogenerated electrons with its Fe^{3+} ions, thus further boosting the efficiency of the photocatalytic process [47].

In this study, we present the synthesis and application of a magnetic Fe$_3$O$_4$/Bi$_2$MoO$_6$/g-C$_3$N$_4$ composite photocatalyst for the efficient degradation of SM under visible light irradiation. The composite was characterized using various techniques, including X-ray diffraction (XRD), scanning electron microscopy (SEM), X-ray photoelectron spectroscopy (XPS), Fourier transform infrared spectroscopy (FT-IR), photoluminescence spectroscopy (PL), UV-vis diffuse reflectance spectra (UV-vis) and the use of a vibrating sample magnetometer (VSM). The photocatalytic performance of the Fe$_3$O$_4$/Bi$_2$MoO$_6$/g-C$_3$N$_4$ composite was evaluated for the degradation of sulfamerazine (SM1). Furthermore, the stability and reusability of the composite photocatalyst were assessed through cyclic degradation experiments. This research contributes to the ongoing efforts to develop highly efficient

and environmentally friendly photocatalysts for the removal of sulfonamide antibiotics from contaminated water sources.

2. Materials and Methods

2.1. Materials

The chemicals used in this study, including urea, $Bi(NO_3)_3 \cdot 5H_2O$, sodium molybdate ($Na_2HPO_4 \cdot 12H_2O$), and sodium hydroxide (NaOH), were sourced from Tianjin Xintong Fine Chemicals Company Limited, Tianjin, China. SM1 and Iron(III) chloride hexahydrate ($FeCl_3 \cdot 6H_2O$) were acquired from Shanghai McLean Biochemical Technology Co., Ltd., Shanghai, China, while polyethylene glycol (PEG) was obtained from Merck Chemical Technology (Shanghai, China) Co., Ltd. All reagents employed in this study were of analytical grade and were used without further purification. Deionized water was used for the preparation of all solutions.

2.2. Preparation of Photocatalyst

2.2.1. Synthesis of g-C_3N_4

The g-C_3N_4 samples were synthesized according to the literature [48]. Briefly, 10 g of urea was heated at 550 °C for 4 h in a covered crucible, resulting in a yellow-colored powder. After cooling, the powder was washed with deionized water and ethanol, dried at 60 °C for 12 h, and calcined at 500 °C for 330 min. The final product was identified as g-C_3N_4.

2.2.2. Synthesis of Bi_2MoO_6

Bi_2MoO_6 was synthesized using a hydrothermal process. Initially, 0.97 g of $Bi(NO_3)_3 \cdot 5H_2O$ and 0.242 g of $Na_2MoO_4 \cdot 12H_2O$ were dissolved in 38 mL of deionized water, followed by stirring with a magnetic stirrer for 1 h and 30 min of ultrasonication to ensure homogeneous dispersion. The pH of the mixture was adjusted to 6 using a 2.0 mol/L NaOH solution, and the solution was stirred for another hour to achieve a uniform suspension. The mixture was subsequently transferred to a hydrothermal reaction vessel and heated at 160 °C for 12 h. Upon the completion of the hydrothermal reaction, the yellow solid was collected by filtration, washed alternatively with ethanol and deionized water several times, and then dried at 60 °C for 24 h.

2.2.3. Synthesis of Fe_3O_4

Magnetic Fe_3O_4 nanoparticles were synthesized using a solvothermal method. Initially, 40 mL of ethylene glycol was mixed with 1.35 g of $FeCl_3 \cdot 6H_2O$, and the solution was stirred until a clear yellow color was achieved. Subsequently, 3.6 g of anhydrous sodium acetate and 1.0 g of polyethylene glycol were added, and the mixture was stirred for 30 min. The resulting solution was transferred to a 100 mL hydrothermal reaction kettle and heated at 200 °C in a convection-drying oven for 8 h. After cooling the kettle to room temperature, the black Fe_3O_4 precipitated particles were collected, washed alternatively with anhydrous ethanol and deionized water three times, and dried in a convection-drying oven at 60 °C for 24 h to obtain the magnetic Fe_3O_4 nanoparticles.

2.2.4. Synthesis of $Fe_3O_4/Bi_2MoO_6/g$-C_3N_4

The Bi_2MoO_6/g-C_3N_4 composite was prepared using a wet-impregnation method. Briefly, 0.3 g of g-C_3N_4 was dispersed in methanol, combined with Bi_2MoO_6, and sonicated for 1h. The composite was collected, washed, and dried at 60 °C for 24 h. The Fe_3O_4 was first dispersed in a mixture of deionized water and anhydrous ethanol by ultrasonication. The prepared Bi_2MoO_6/g-C_3N_4 was added and mixed for 2 h, followed by further ultrasonication. The mixture was transferred to a hydrothermal reaction kettle and heated at 180 °C for 8 h. The resulting black solution was washed with anhydrous ethanol and deionized water and dried at 60 °C for 24 h to obtain the $Fe_3O_4/Bi_2MoO_6/g$-C_3N_4 composite. The ratio of Bi_2MoO_6 to g-C_3N_4 is 1:32, and the ratio of Fe_3O_4 to the Bi_2MoO_6/g-C_3N_4 is 1:8.

2.3. Characterization

An XRD analysis was conducted utilizing a Rigaku Ultima IV diffractometer with Cu Kα radiation, scanning the 2θ range between 10 and 90°. SEM images were acquired using a FEI Quanta-PEG 450 microscope. The XPS measurements were carried out using a Thermo VG ESCALAB-250 under A1Kα (1486.6 eV) radiation. PL measurements were performed with an F-98 system (Shanghai, China), and FT-IR spectroscopy was carried out using a PerkinElmer Spectrum Two spectrometer. UV-vis spectroscopy measurements were obtained using a TU-1901 spectrophotometer (Beijing, China), covering a wavelength range of 200–800 nm. The magnetic properties were determined using a VSM (Lake Shore).

2.4. Photocatalytic Experiments

The photocatalytic degradation of SM1 by the $Fe_3O_4/Bi_2MoO_6/g-C_3N_4$ samples was examined under irradiation using a 500 W xenon lamp equipped with a 420 nm cut-off filter. An SM1 solution (3 mg/L) was prepared, to which 800 mg of the synthesized photocatalysts was added, followed by dilution to a final volume of 50 mL. To establish an adsorption/desorption equilibrium between SM1 and the photocatalysts, the suspensions were magnetically stirred in the dark for 30 min before irradiation commenced. At regular intervals, 1.5 mL aliquots of the suspension were extracted and filtered through a 0.22 μm filter (Millipore) to determine the residual SM1 concentration. The concentration of SM1 was quantified via HPLC (Agilent Technologies 1200-Series). To assess the stability and reusability of the photocatalyst, cyclic experiments of SM1 photodegradation were conducted. The catalyst stability was determined after many reaction cycles in which the catalysts were collected magnetically and washed with deionized water before the next cycle.

3. Results and Discussion

3.1. Characterization

The results of the XRD analysis of the $g-C_3N_4$, Bi_2MoO, Fe_3O_4 and $Fe_3O_4/Bi_2MoO_6/g-C_3N_4$ prepared in this study are depicted in Figure 1. The XRD patterns of $g-C_3N_4$ exhibit well-defined diffraction peaks at 2θ values of approximately 13.0° and 27.4°. The diffraction peak located near 13.0° corresponds to the (100) plane of $g-C_3N_4$, while the peak observed around 27.4° is attributed to the (002) plane of $g-C_3N_4$. These peak positions are in good agreement with the characteristic XRD patterns of $g-C_3N_4$ (JCPDS 87-1526) [49]. For the Bi_2MoO_6 sample, distinct characteristic peaks are observed at 2θ values of 27.361°, 31.705°, 32.562°, 45.481°, 53.905°, 56.441°, and 66.429°. These peaks correspond to the (131), (200), (151), (202), (331), (262), and (004) planes of the orthorhombic Bi_2MoO_6 phase, as referenced in the standard card (JCPDS 76-2388) [50]. In the case of the Fe_3O_4 sample, well-defined characteristic peaks are observed at 2θ values of 30.206°, 35.501°, 43.190°, 53.717°, 57.221°, and 62.738°. These peaks correspond to the (220), (311), (400), (422), (511), and (440) planes of Fe_3O_4, as indicated in the standard card (JCPDS 19-0629) [51]. The $Fe_3O_4/Bi_2MoO_6/g-C_3N_4$ diffraction pattern clearly reveals the presence of the $g-C_3N_4$ (002) plane, the Bi_2MoO_6 (131), (200), (151), and (202) planes, and the Fe_3O_4 (220), (311), (400), (422), (511), and (440) planes. Moreover, the diffraction peaks of Bi_2MoO_6 and Fe_3O_4 remain unshifted, suggesting that the loading of Bi_2MoO_6 and Fe_3O_4 onto the $g-C_3N_4$ surface does not modify their respective crystal structures. The diffraction pattern is devoid of any additional impurity peaks, implying that the reaction did not produce new impurities and that the synthesized magnetic photocatalyst composite exhibits a high level of purity. Furthermore, the intensities of the Fe_3O_4 diffraction peaks in the $Fe_3O_4/Bi_2MoO_6/g-C_3N_4$ sample are marginally lower compared to those of the pure Fe_3O_4 diffraction peaks, indicating the presence of interactions between Fe_3O_4 and the $Bi_2MoO_6/g-C_3N_4$ composite.
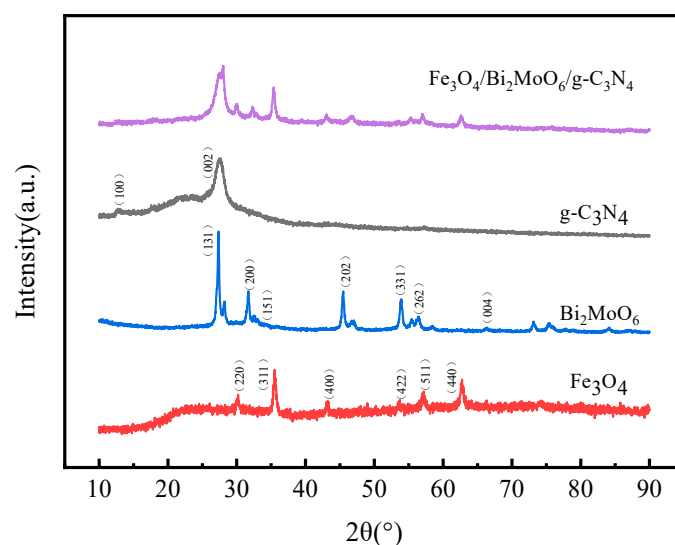
Figure 1. XRD patterns of g-C_3N_4, Bi_2MoO_6, Fe_3O_4, and Fe_3O_4/Bi_2MoO_6/g-C_3N_4.

As depicted in Figure 2a, the g-C_3N_4 synthesized using the thermal oxidation exfoliation method with urea as a precursor resulted in a profusion of irregularly stacked lamellar structures. These layered architectures play a critical role in facilitating shorter electron transfer pathways, thereby promoting the efficient migration of photogenerated charge carriers. Moreover, the enhanced specific surface area and pore volume offer a greater number of active sites for photocatalytic reactions, which could lead to improved photocatalytic performance. Figure 2b illustrates the Bi_2MoO_6 synthesized via the hydrothermal method. The sample exhibits a stacked, block-like morphology with an estimated block size ranging from approximately 200 to 400 nm. Notably, the presence of significant agglomeration within the sample is observed, which could impact the photocatalytic efficiency due to the increased surface area for reactions to occur on. In Figure 2c, Fe_3O_4 nanospheres are presented, which have been synthesized using the solvothermal technique. These nanospheres display favorable dispersibility, which can be attributed to their relatively small dimensions. This characteristic may contribute to a more uniform distribution of active sites and improved accessibility for reactants, leading to enhanced photocatalytic performance. Figure 2d demonstrates that the Fe_3O_4 nanospheres are well-dispersed across the surface of the Bi_2MoO_6/g-C_3N_4 composite. The integration of Fe_3O_4 into the composite not only enables rapid photocatalyst recovery due to its magnetic properties but also contributes to improved electron migration rates owing to its exceptional electronic conductivity. Furthermore, the presence of Fe_3O_4 may reduce the recombination of photogenerated electron–hole pairs, thereby increasing the photocatalytic efficiency of the composite material. Overall, the enhanced material properties and morphological characteristics of the Fe_3O_4/Bi_2MoO_6/g-C_3N_4 composite are expected to result in good photocatalytic performance.

As illustrated in Figure 3, the Fe_3O_4/Bi_2MoO_6/g-C_3N_4 composites with varying ratios display pronounced absorption peaks in the regions of 810 cm^{-1}, 1200–1700 cm^{-1}, and 3200–3400 cm^{-1}, which are in line with the absorption peaks observed for the pure g-C_3N_4. The distinct absorption peak situated around 810 cm^{-1} can be attributed to the bending vibrations associated with the 3-s-triazine ring [52]. The multiple absorption peaks that emerge between 1200 and 1700 cm^{-1} are likely a result of stretching vibrations pertaining to C-N and C=N heterocyclic rings [53]. Furthermore, the broad absorption peak in the range of 3200–3400 cm^{-1} may arise due to the stretching vibrations of the NH and NH$_2$ functional groups or the O-H stretching vibrations present in H$_2$O molecules [54]. These observations suggest that the g-C_3N_4 structure remains intact during the composite formation process, corroborating the findings from the XRD characterization. Significant variations in the FT-IR spectrum of Bi_2MoO_6 are mainly observed between 400 and 900 cm^{-1}. The absorption

peaks detected between 732 and 841 cm^{-1} primarily stem from the stretching vibrations of Mo-O bonds. In contrast, the absorption peaks between 450 and 565 cm^{-1} result from the stretching and deformation vibrations related to Bi-O bonds [55]. The absorption peak near 3400 cm^{-1}, which is induced by O-H vibrations, coincides with the corresponding peak for g-C$_3$N$_4$. The Fe$_3$O$_4$/Bi$_2$MoO$_6$/g-C$_3$N$_4$ composite reveals a characteristic Fe-O stretching vibration of Fe$_3$O$_4$ around 589 cm^{-1} [56]. This observation suggests an enhancement in the absorption peak of surface-adsorbed O-H groups and an increase in the density of hydroxyl on the Fe$_3$O$_4$/Bi$_2$MoO$_6$/g-C$_3$N$_4$ composite surface. Consequently, these factors contribute to the improvement of the adsorption performance for the photocatalyst. This evidence implies that the photocatalyst formation is not a mere aggregation of components; instead, it involves interactions mediated by intermolecular forces.
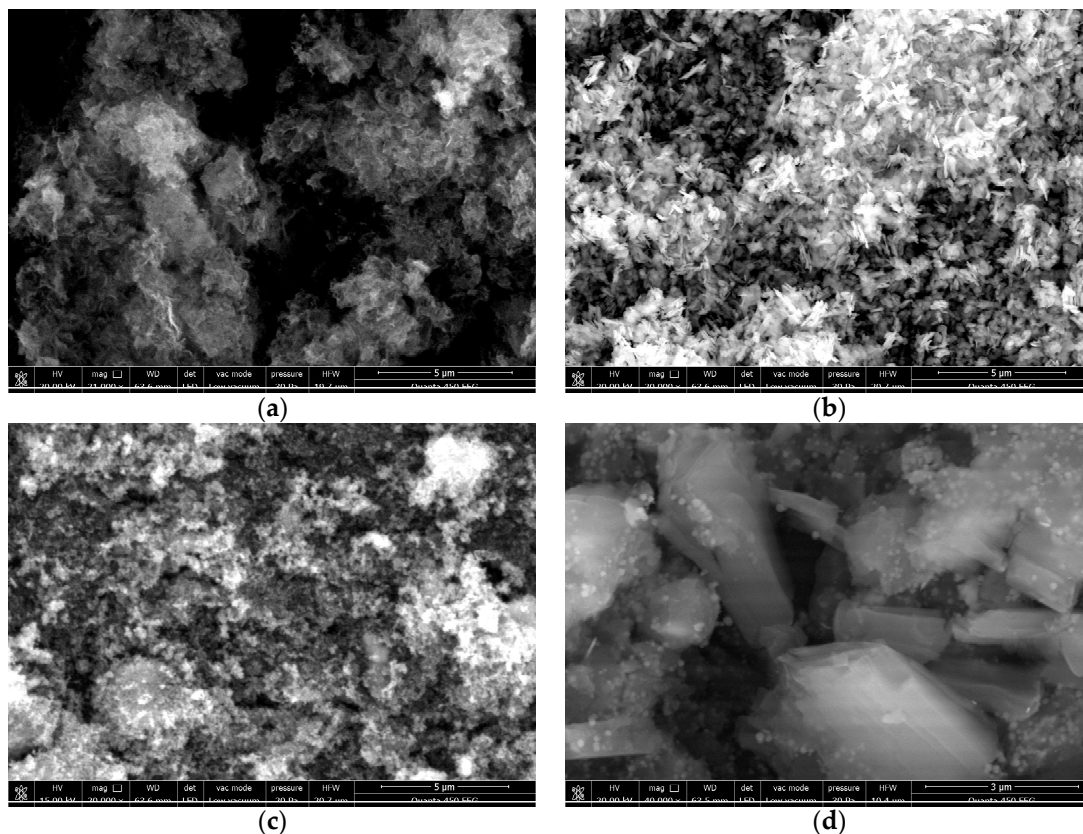

Figure 2. SEM images of (**a**) g-C$_3$N$_4$, (**b**) Bi$_2$MoO$_6$ (**c**) Fe$_3$O$_4$, and (**d**) Fe$_3$O$_4$/Bi$_2$MoO$_6$/g-C$_3$N$_4$.

To further verify the chemical compositions of the magnetic composite photocatalysts and investigate the interplay between the -C$_3$N$_4$ nanosheets, Bi$_2$MoO$_6$, and Fe$_3$O$_4$ nanospheres, XPS was utilized to analyze their chemical compositions, chemical bonds, and chemical binding states. Figure 4 presents the XPS survey spectra for g-C$_3$N$_4$, Bi$_2$MoO$_6$, the Fe$_3$O$_4$ nanospheres, and the Fe$_3$O$_4$/Bi$_2$MoO$_6$/g-C$_3$N$_4$ composite. The g-C$_3$N$_4$ nanosheets are primarily composed of carbon and nitrogen elements, with oxygen originating from oxygen-containing compounds adsorbed on the sample surface. Bi$_2$MoO$_6$ consists of carbon, oxygen, bismuth, and molybdenum elements. In contrast, Fe$_3$O$_4$ is formed from carbon, oxygen, and iron elements. The Fe$_3$O$_4$/Bi$_2$MoO$_6$/g-C$_3$N$_4$ magnetic composite photocatalyst encompasses carbon, nitrogen, oxygen, bismuth, molybdenum, and iron elements, signifying the presence of all three constituents: g-C$_3$N$_4$ nanosheets, Bi$_2$MoO$_6$, and Fe$_3$O$_4$ nanospheres. This finding corroborates the results obtained from the FT-IR characterization.
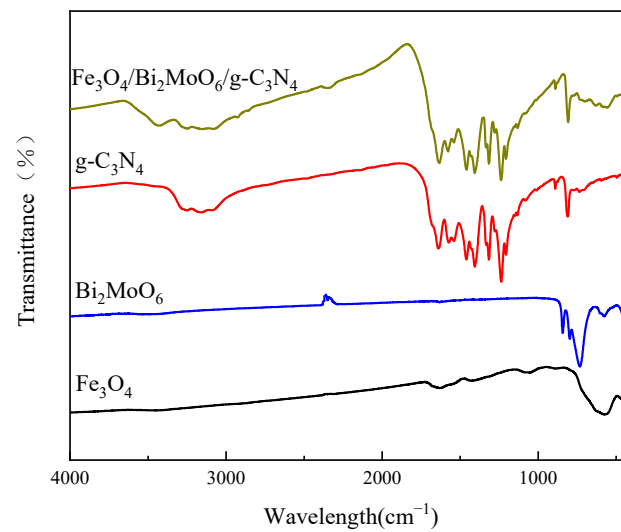
Figure 3. FT-IR spectra of g-C_3N_4, Bi_2MoO_6, Fe_3O_4, and Fe_3O_4/Bi_2MoO_6/g-C_3N_4.
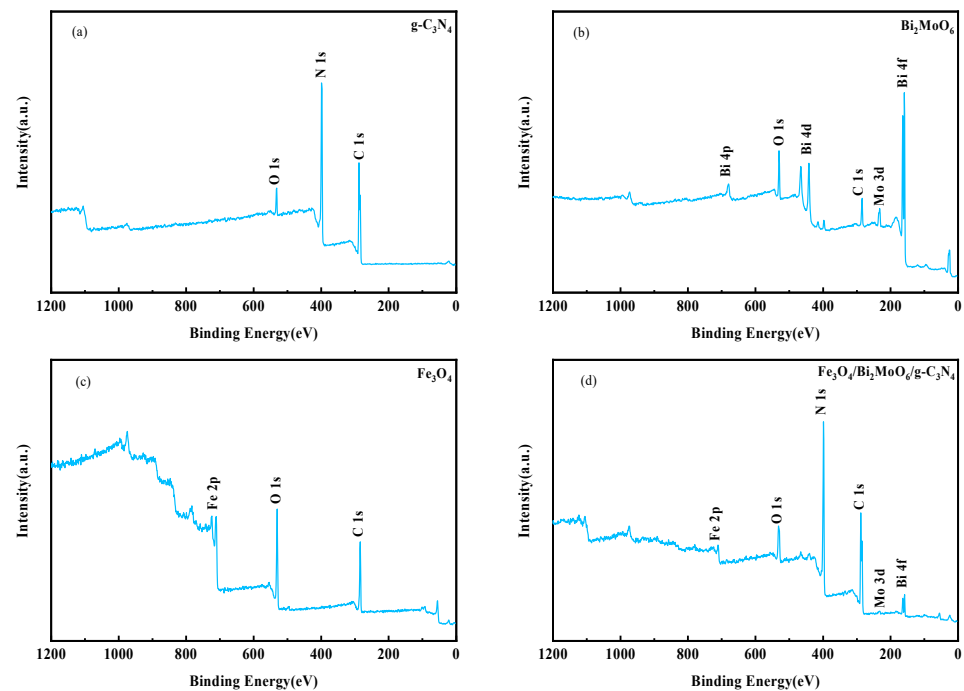
Figure 4. XPS survey spectra of (**a**) g-C_3N_4, (**b**) Bi_2MoO_6, (**c**) Fe_3O_4, and (**d**) Fe_3O_4/Bi_2MoO_6/g-C_3N_4.

Figure 5 presents the XPS spectra for C 1s, N 1s, O 1s, Bi 4f, Mo 3d, and Fe 2p. Each sample's binding energy is calibrated using the C 1s standard binding energy (284.8 eV). In Figure 5a, the C 1s spectra of the Fe_3O_4/Bi_2MoO_6/g-C_3N_4 sample exhibit characteristic peaks at 284.8 eV, 286.3 eV, and 288.3 eV, corresponding to the C-C, C-O, and N=C-N chemical bonds [57,58],. Figure 5b displays the N 1s spectra with three distinct peaks at 398.8 eV (C–N–C), 400.1 eV (N-(C)$_3$), and 401.2 eV (N–H groups) [59], with no significant alterations compared to the g-C_3N_4 sample. In Figure 5c, the O 1s spectra of the Fe_3O_4/Bi_2MoO_6/g-C_3N_4 sample present three characteristic peaks at 529.6 eV (OL), 532.0 eV (C-O), and 533.6 eV (C=O) [60]. The intensity at 532.3 eV reduces to 532.0 eV, while the intensity at 533.6 eV remains constant. This change suggests interactions between g-C_3N_4 and the other components (Fe_3O_4 and Bi_2MoO_6) in the composite, causing a shift in the binding energy of the oxygen atoms associated with the C-O bond. Figure 5d,e depict the Bi 4f and Mo 3d high-resolution spectra for the Bi_2MoO_6 and Fe_3O_4/Bi_2MoO_6/g-C_3N_4

samples, revealing slight decreases in peak intensities, indicating consistent binding energies and the occurrence of chemical bonding or strong electrostatic interactions between the photocatalysts [61]. In Figure 5f, the Fe 2p spectra of the Fe_3O_4 sample exhibit two characteristic peaks at 710.3 eV and 723.4 eV, corresponding to Fe $2p_{3/2}$ and Fe $2p_{1/2}$ orbitals of Fe^+ [62]. The $Fe_3O_4/Bi_2MoO_6/g\text{-}C_3N_4$ sample shows reduced peak intensities at 709.6 eV and 722.8 eV, confirming the successful interaction and combination of Fe_3O_4, Bi_2MoO_6, and $g\text{-}C_3N_4$ in the photocatalyst.
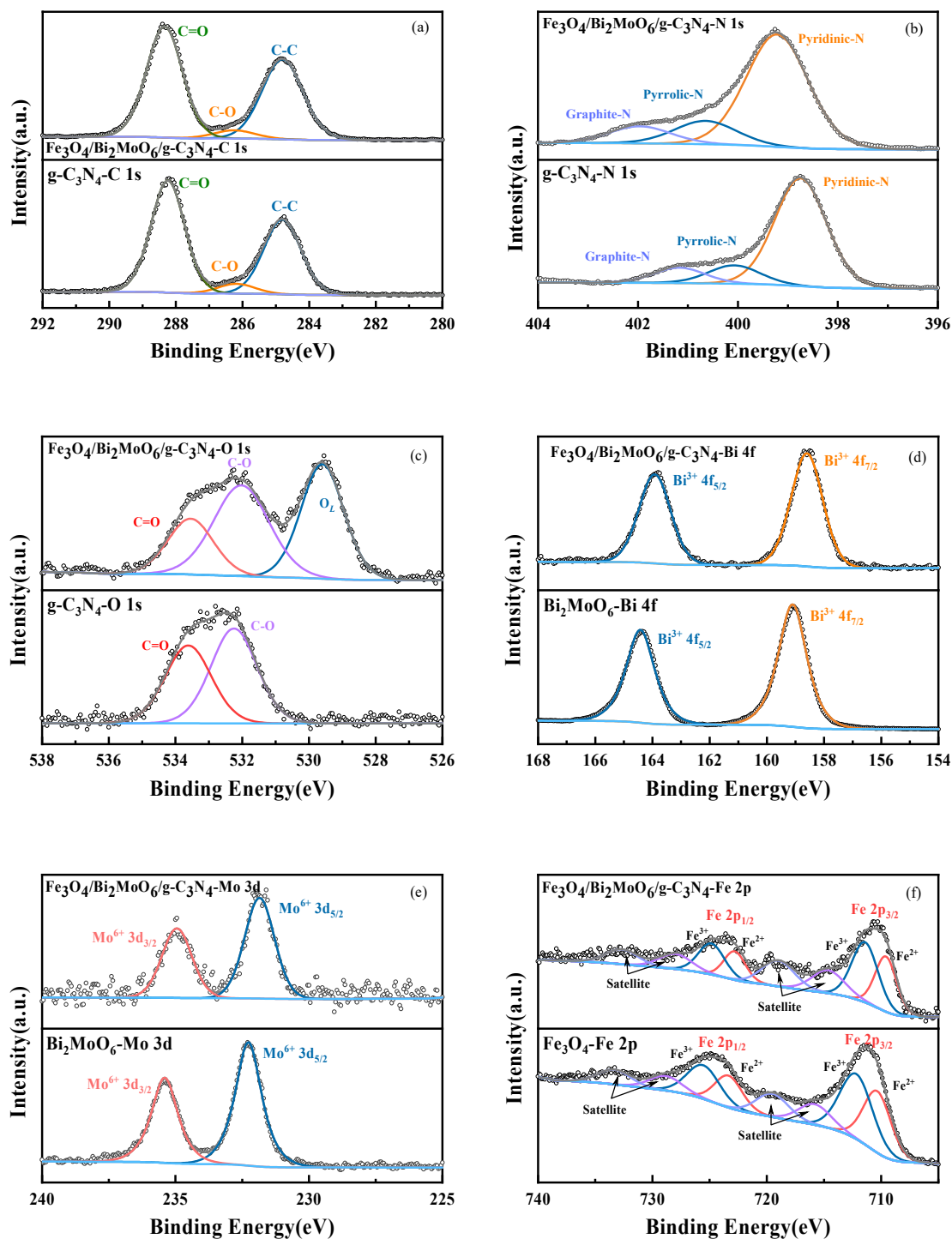

Figure 5. XPS spectra of $Fe_3O_4/Bi_2MoO_6/g\text{-}C_3N_4$ in (**a**) C 1s, (**b**) N 1s, (**c**) O 1s, (**d**) Bi 4f, (**e**) Mo 3d, and (**f**) Fe 2p.

The use of PL emission spectra is a widely adopted technique for evaluating the efficiency of photogenerated electron–hole pair separation in various materials. As depicted in Figure 6, the fluorescence intensities can be arranged in descending order as follows: $g\text{-}C_3N_4$ > Fe_3O_4 > Bi_2MoO_6 > $Fe_3O_4/Bi_2MoO_6/g\text{-}C_3N_4$. The observed fluorescence intensities for the $Fe_3O_4/Bi_2MoO_6/g\text{-}C_3N_4$ composites are lower than those of their individual constituents, $g\text{-}C_3N_4$, Fe_3O_4, and Bi_2MoO_6. This finding implies that the formation of composite photocatalysts leads to a significant reduction in the recombination rate of the photogenerated electron–hole pairs. Additionally, the spectral data suggest that Fe_3O_4 inherently possesses favorable electronic conductivity, which facilitates the migration of photogenerated charge carriers. Consequently, the improved charge separation and migration contribute to the enhanced photocatalytic performance of the composite materials.
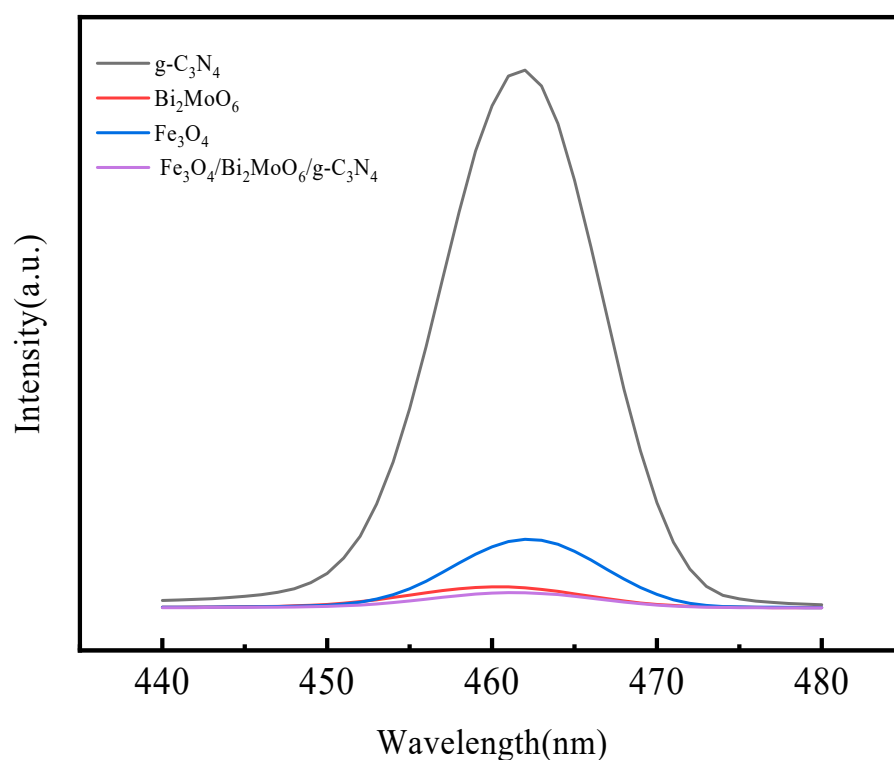

Figure 6. PL spectra of $g\text{-}C_3N_4$, Bi_2MoO_6, Fe_3O_4, and $Fe_3O_4/Bi_2MoO_6/g\text{-}C_3N_4$.

The photocatalytic activity of a material is predominantly influenced by its capacity to absorb and exploit incident light. In order to investigate the optical absorption characteristics of the magnetic composite photocatalyst $Fe_3O_4/Bi_2MoO_6/g\text{-}C_3N_4$, UV-vis diffuse reflectance spectroscopy was employed. As depicted in Figure 7, all samples exhibit a degree of light absorption capacity within the ultraviolet range, as well as a discernable response within the visible light range. This behavior is primarily governed by the samples' bandgap width. The as-synthesized $g\text{-}C_3N_4$ demonstrates an absorption edge at approximately 438 nm, while the Bi_2MoO_6 sample exhibits an absorption edge at approximately 460 nm. According to the prior literature [63], the primary absorption wavelength of Fe_3O_4 resides within the ultraviolet light region. Upon the incorporation of Fe_3O_4, the absorption edge for the $Fe_3O_4/Bi_2MoO_6/g\text{-}C_3N_4$ composite is observed at approximately 710 nm, which further expands the response range within the visible light domain. According to the Kubelka–Munk function, the bandgaps of the $g\text{-}C_3N_4$, Bi_2MoO_6, Fe_3O_4, and $Fe_3O_4/Bi_2MoO_6/g\text{-}C_3N_4$ are 2.96 eV, 3.03 eV, 1.16 eV, and 2.80 eV, respectively. The bandgap energy of a material is closely associated with its absorption properties and therefore its photocatalytic performance. When the aforementioned materials are combined to form $Fe_3O_4/Bi_2MoO_6/g\text{-}C_3N_4$, the composite material presents a bandgap of 2.80 eV, slightly smaller than those of $g\text{-}C_3N_4$ and Bi_2MoO_6 yet significantly larger than the bandgap

of Fe_3O_4. This composite behavior results in an enhanced absorption of light, especially in the visible region, as is evident from the absorption edge observed at approximately 710 nm. The results highlight the synergistic effect of the three components in which Fe_3O_4 effectively extends the light absorption to the visible range, while the wide bandgap materials (g-C_3N_4 and Bi_2MoO_6) contribute to the overall photocatalytic performance under UV light. Consequently, the composite photocatalyst exhibits an enhanced capability to generate active species under identical illumination conditions, which ultimately leads to its improved photocatalytic performance.
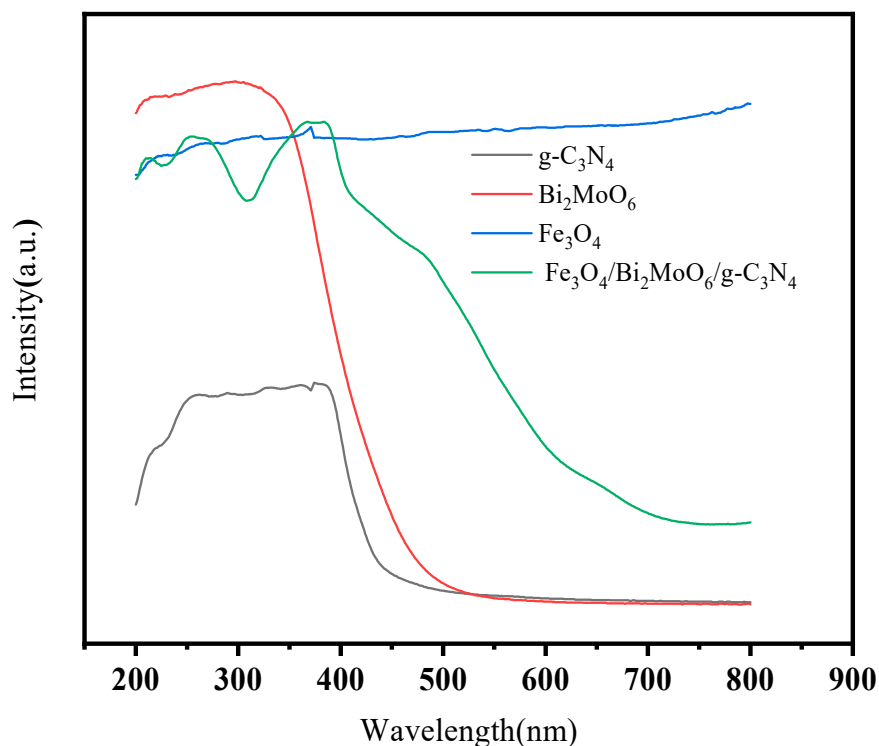

Figure 7. UV–Vis DRS spectra of g-C_3N_4, Bi_2MoO_6, Fe_3O_4, and $Fe_3O_4/Bi_2MoO_6/g$-C_3N_4.

As depicted in Figure 8, the magnetic hysteresis loops for Fe_3O_4 and $Fe_3O_4/Bi_2MoO_6/$ g-C_3N_4 are illustrated. Employing the solvothermal method, the synthesized Fe_3O_4 nanospheres possess dimensions exceeding the critical size threshold for superparamagnetism, thereby conferring ferromagnetic characteristics to the $Fe_3O_4/Bi_2MoO_6/g$-C_3N_4 composite material. The saturation magnetization and coercivity values for the Fe_3O_4 are determined to be 74.32 emu/g and 50.74 Oe, respectively. In contrast, the $Fe_3O_4/Bi_2MoO_6/$ g-C_3N_4 composite exhibits a saturation magnetization of 7.24 emu/g and a coercivity of 5.49 Oe. Owing to the relatively smaller proportion of Fe_3O_4 in the magnetic composite photocatalyst, the magnetization strength decreases in comparison to that of the pristine Fe_3O_4 nanoparticles. Nevertheless, the $Fe_3O_4/Bi_2MoO_6/g$-C_3N_4 composite demonstrates favorable ferromagnetic and magnetic recovery properties, indicating its potential applicability for efficient magnetic separation and recycling in photocatalytic processes. This finding emphasizes the necessity of optimizing the compositions of magnetic composite photocatalysts to achieve a balance between desirable magnetic properties and overall photocatalytic performance.
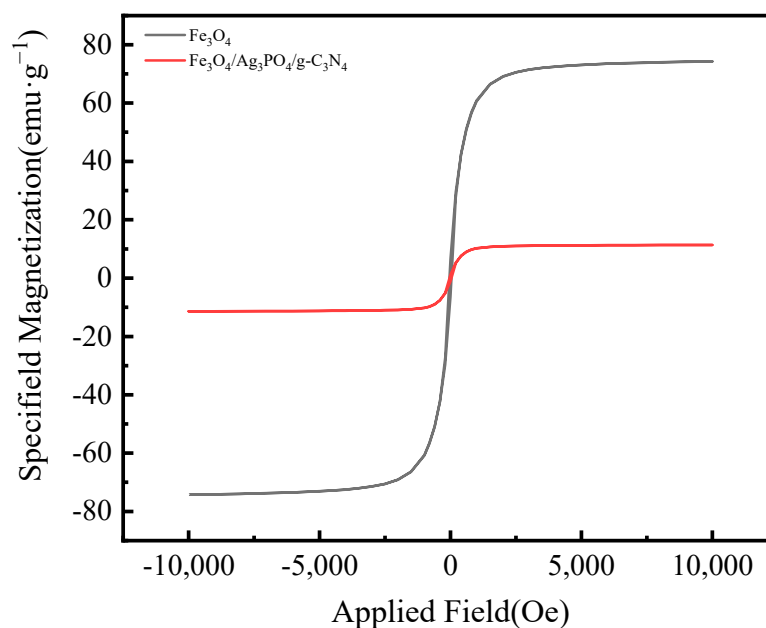
Figure 8. VSM spectra of Fe_3O_4 and $Fe_3O_4/Bi_2MoO_6/g\text{-}C_3N_4$.

### 3.2. Photocatalyst Performance Analysis

Due to the inherent stability of SM1, its degradation under visible light without a photocatalyst presents a significant challenge. Following 120 min of visible light irradiation, the photocatalysts in the dark condition demonstrated a minimal removal efficiency for SM1 at less than 5%. This observation suggests that the adsorption by the photocatalysts can be largely disregarded in the overall process. To investigate the influence of solution pH on the degradation of SM1 under visible light using $Fe_3O_4/Bi_2MoO_6/g\text{-}C_3N_4$, photocatalytic experiments were conducted with initial pH values adjusted to 5.0, 6.0, 7.0, 8.0, and 9.0. Figure 9a demonstrates that when the initial pH of the sulfonamide antibiotic solution ranged from 5.0 to 8.0, no significant changes were observed in the photodegradation efficiency of SM1. However, at a pH of 9.0, the photodegradation efficiency of SM1 markedly increased. At pH values of 5.0, 6.0, 7.0, 8.0, and 9.0, the degradation efficiencies of SM1 by $Fe_3O_4/Bi_2MoO_6/g\text{-}C_3N_4$ within 120 min were 63.23%, 74.22%, 73.68%, 81.91%, and 95.58%, respectively. As depicted in Figure 9b, the degradation kinetic constants at pH values of 5.0, 6.0, 7.0, 8.0, and 9.0 were 0.00839, 0.01082, 0.01032, 0.01358, and 0.02574 min^{-1}, respectively. Within the pH range of 5.0 to 8.0, the observed stability could be attributed to the different species of SM1 present at various pH values having similar reactivities with the generated OH· radicals. However, a significant increase in degradation efficiency at a pH of 9.0 suggests that the interaction between the generated OH· radicals and the dominant anionic species of SM1 at this pH value may result in a more effective degradation process. Moreover, the increased concentrations of OH- ions (or the availability of H_2O molecules) at higher pH values could contribute to the enhanced generation of active species, leading to improvements in the photodegradation performance.

The photochemical stability of a photocatalyst is a critical factor in determining its suitability for practical applications. To evaluate the stability of the $Fe_3O_4/Bi_2MoO_6/g\text{-}C_3N_4$ magnetic composite photocatalyst, five consecutive photocatalytic degradation cycles of SM1 were performed under identical experimental conditions. As shown in Figure 10a, the solution pH was adjusted to 9. The visible light degradation rate of SM1 was monitored within a 120 min time frame. In the five degradation cycles, the degradation rates were 95.58%, 93.70%, 91.77%, 89.82%, and 87.86%, respectively. With the increasing number of recovery cycles of the $Fe_3O_4/Bi_2MoO_6/g\text{-}C_3N_4$ magnetic composite photocatalyst, the degradation rate of SM1 decreased slightly. However, the rate tended to stabilize as the number of recovery cycles increased. After five cycles, the degradation rate remained

above 87%, indicating no significant decrease in performance. This demonstrates that the $Fe_3O_4/Bi_2MoO_6/g\text{-}C_3N_4$ magnetic composite photocatalyst retains its effective photocatalytic degradation capabilities and recyclability after multiple cycles, confirming its stable photocatalytic performance. Following the five consecutive cycles, the catalyst sample was filtered, dried, and analyzed using XRD. Figure 10b reveals no apparent changes in the composition or chemical structure of the $Fe_3O_4/Bi_2MoO_6/g\text{-}C_3N_4$ magnetic composite photocatalyst, providing evidence of its chemical stability.
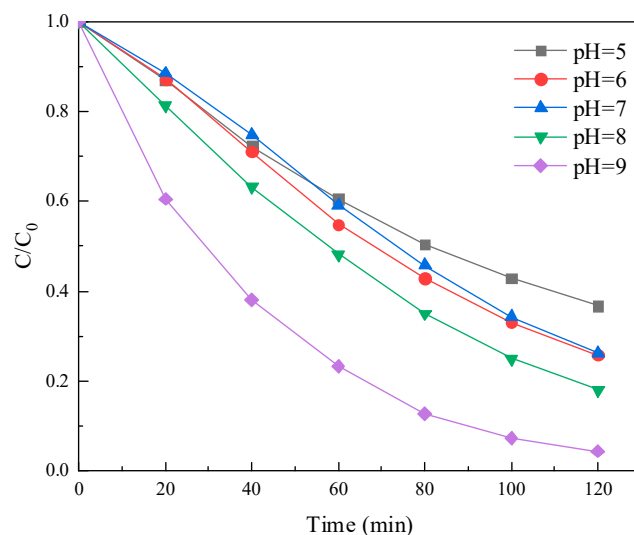
(a)
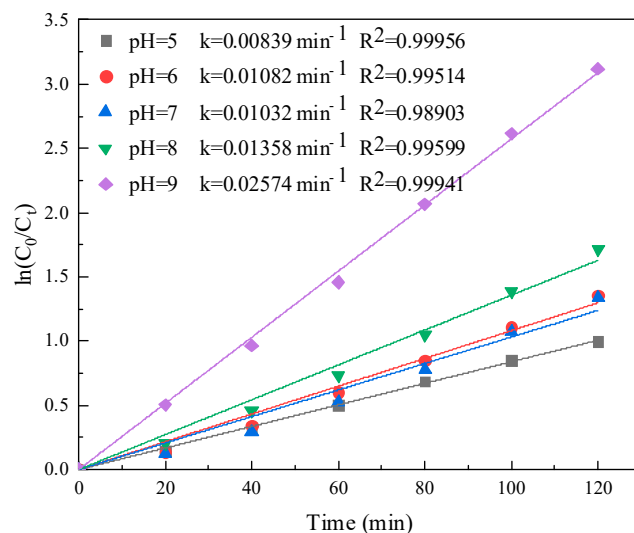
(b)

**Figure 9.** (**a**) Photocatalytic efficiencies of $Fe_3O_4/Bi_2MoO_6/g\text{-}C_3N_4$ with different pH for SM1 under visible light irradiation. (**b**) Plots of $\ln(C_0/C_t)$ versus irradiation time for SM1.

It is worth noting that the consistent photocatalytic performance can be attributed to several factors, including the robustness of the composite material, effective charge separation and transfer, and the resistance to photocorrosion. The incorporation of Fe_3O_4 in the composite not only enhances the magnetic properties but also contributes to the stability of the material by improving electron conductivity. In future studies, a more comprehensive

investigation could be performed to examine the possible degradation of the catalyst's surface and structural alterations and potential changes in the active sites after extended usage. Such assessments would further contribute to our understanding of the catalyst's long-term stability and its potential for practical applications in environmental remediation.
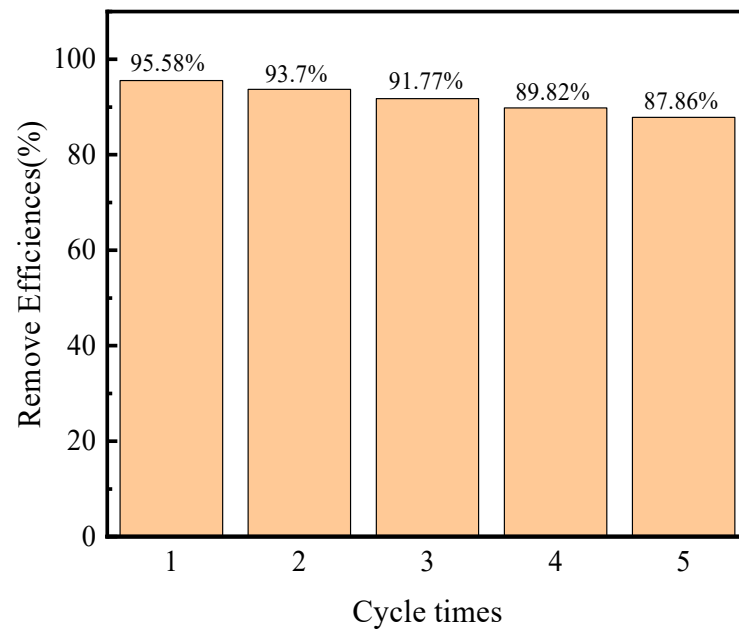
(**a**)
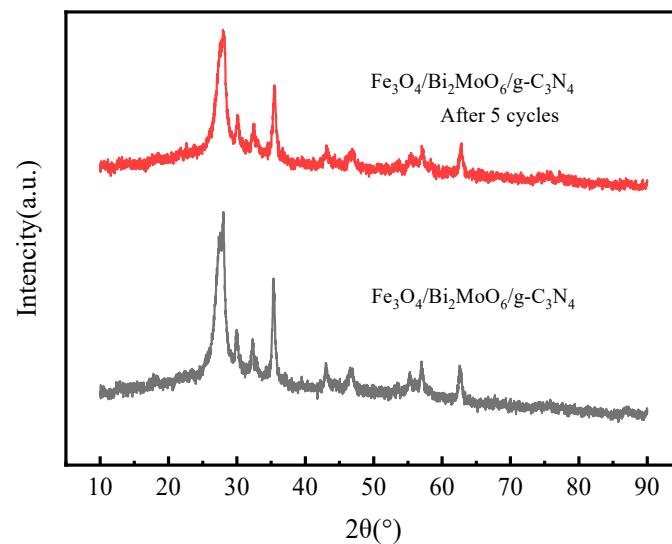
(**b**)

Figure 10. (**a**) Stability and reusability test; (**b**) XRD pattern of $Fe_3O_4/Bi_2MoO_6/g\text{-}C_3N_4$ of after reaction.

4. Conclusions

In summary, this study presents a comprehensive investigation into the synthesis, characterization, and application of a $Fe_3O_4/Bi_2MoO_6/g\text{-}C_3N_4$ magnetic composite photocatalyst for the visible-light-driven photocatalytic degradation of sulfonamide antibiotics, with a particular focus on SM1. The findings highlight the importance of solution pH in the degradation process, which influences not only the speciation of sulfonamides, transitioning between cationic, molecular, and anionic forms, but also the generation of reactive species such as hydroxyl radicals that are crucial for effective degradation. Through a series of carefully designed experiments, the study revealed that optimal photocatalytic perfor-

mance was achieved at a pH value of 9.0. Moreover, the $Fe_3O_4/Bi_2MoO_6/g\text{-}C_3N_4$ magnetic composite photocatalyst exhibited exceptional stability and recyclability, maintaining a high degradation efficiency of over 87% after five consecutive cycles. An XRD analysis conducted after the cycling tests confirmed that the composite's composition and chemical structure remained unchanged, further supporting its chemical stability. This comprehensive investigation not only contributes valuable insights into the photocatalytic degradation of sulfonamide antibiotics using magnetic composite photocatalysts but also underscores the potential of the $Fe_3O_4/Bi_2MoO_6/g\text{-}C_3N_4$ magnetic composite for practical applications in environmental remediation. To further advance this research and its potential impact, future studies could explore the long-term stability and performance of the catalyst under a broader range of operational conditions. Additionally, in-depth investigations into potential degradation pathways and mechanisms could provide a deeper understanding of the catalyst's applicability and its effectiveness in addressing complex water pollution challenges. Overall, the findings of this study pave the way for the development of more efficient and sustainable strategies for water treatment and pollution control.

References

1. Liu, J.-L.; Wong, M.-H. Pharmaceuticals and personal care products (PPCPs): A review on environmental contamination in China. *Environ. Int.* **2013**, *59*, 208–224. [CrossRef]
2. Dey, S.; Bano, F.; Malik, A. Pharmaceuticals and personal care product (PPCP) contamination—A global discharge inventory. In *Pharmaceuticals and Personal Care Products: Waste Management and Treatment Technology*; Elsevier: Amsterdam, The Netherlands, 2019; pp. 1–26.
3. Yang, L.; Wang, T.; Zhou, Y.; Shi, B.; Bi, R.; Meng, J. Contamination, source and potential risks of pharmaceuticals and personal products (PPCPs) in Baiyangdian Basin, an intensive human intervention area, China. *Sci. Total Environ.* **2021**, *760*, 144080. [CrossRef] [PubMed]
4. Wang, C.; Lu, Y.; Sun, B.; Zhang, M.; Wang, R.; Li, X.; Mao, R.; Cao, Z.; Song, S. Contamination, transport, and ecological risks of pharmaceuticals and personal care products in a large irrigation region. *Sci. Total Environ.* **2022**, *851*, 158179. [CrossRef] [PubMed]
5. Rienzie, R.; Ramanayaka, S.; Adassooriya, N.M. Nanotechnology applications for the removal of environmental contaminants from pharmaceuticals and personal care products. In *Pharmaceuticals and Personal Care Products: Waste Management and Treatment Technology*; Elsevier: Amsterdam, The Netherlands, 2019; pp. 279–296.
6. Li, N.; Wang, Y.; Li, W.; Li, H.; Yang, L.; Wang, J.; Mahdy, H.A.; Mehany, A.B.; Jaiash, D.A.; Santali, E.Y. Screening of some sulfonamide and sulfonylurea derivatives as anti-Alzheimer's agents targeting BACE1 and PPARγ. *J. Chem.* **2020**, *2020*, 1–19. [CrossRef]
7. Navia, M.A. A chicken in every pot, thanks to sulfonamide drugs. *Science* **2000**, *288*, 2132–2133. [CrossRef]
8. Ovung, A.; Bhattacharyya, J. Sulfonamide drugs: Structure, antibacterial property, toxicity, and biophysical interactions. *Biophys. Rev.* **2021**, *13*, 259–272. [CrossRef]

9.   Tai, Y.; Tam, N.F.-Y.; Ruan, W.; Yang, Y.; Yang, Y.; Tao, R.; Zhang, J. Specific metabolism related to sulfonamide tolerance and uptake in wetland plants. *Chemosphere* **2019**, *227*, 496–504. [CrossRef]

10.   Leal, C.S.; Mesquita, D.P.; Amaral, A.L.; Amaral, A.M.; Ferreira, E.C. Environmental impact and biological removal processes of pharmaceutically active compounds: The particular case of sulfonamides, anticonvulsants and steroid estrogens. *Crit. Rev. Environ. Sci. Technol.* **2020**, *50*, 698–742. [CrossRef]

11.   Baran, W.; Adamek, E.; Ziemiańska, J.; Sobczak, A. Effects of the presence of sulfonamides in the environment and their influence on human health. *J. Hazard. Mater.* **2011**, *196*, 1–15. [CrossRef]

12.   Lee, J.-C.; Jang, J.K.; Kim, H.-W. Sulfonamide degradation and metabolite characterization in submerged membrane photobiore-actors for livestock excreta treatment. *Chemosphere* **2020**, *261*, 127604. [CrossRef]

13.   Yang, C.-W.; Hsiao, W.-C.; Chang, B.-V. Biodegradation of sulfonamide antibiotics in sludge. *Chemosphere* **2016**, *150*, 559–565. [CrossRef] [PubMed]

14.   Luo, B.; Huang, G.; Yao, Y.; An, C.; Zhang, P.; Zhao, K. Investigation into the influencing factors and adsorption characteristics in the removal of sulfonamide antibiotics by carbonaceous materials. *J. Clean. Prod.* **2021**, *319*, 128692. [CrossRef]

15.   Larsson, D.J.; de Pedro, C.; Paxeus, N. Effluent from drug manufactures contains extremely high levels of pharmaceuticals. *J. Hazard. Mater.* **2007**, *148*, 751–755. [CrossRef] [PubMed]

16.   Xu, J.; Xu, Y.; Wang, H.M.; Guo, C.S.; Qiu, H.Y.; He, Y.; Zhang, Y.; Li, X.C.; Meng, W. Occurrence of antibiotics and antibiotic resistance genes in a sewage treatment plant and its effluent-receiving river. *Chemosphere* **2015**, *119*, 1379–1385. [CrossRef]

17.   Zhang, Z.; Zada, A.; Cui, N.; Liu, N.; Liu, M.; Yang, Y.; Jiang, D.; Jiang, J.; Liu, S. Synthesis of ag loaded ZnO/BiOCl with high photocatalytic performance for the removal of antibiotic pollutants. *Crystals* **2021**, *11*, 981. [CrossRef]

18.   González-Poggini, S.; Rosenkranz, A.; Colet-Lagrille, M. Two-dimensional nanomaterials for the removal of pharmaceuticals from wastewater: A critical review. *Processes* **2021**, *9*, 2160. [CrossRef]

19.   Gan, W.; Fu, X.C.; Guo, J.; Zhang, M.; Li, D.D.; Ding, C.S.; Lu, Y.Q.; Wang, P.; Sun, Z.Q. Ag nanoparticles decorated 2D/2D TiO$_2$/g-C$_3$N$_4$ heterojunction for efficient removal of tetracycline hydrochloride: Synthesis, degradation pathways, and mechanism. *Appl. Surf. Sci.* **2022**, *606*, 154837. [CrossRef]

20.   Mahmood, A.; Irfan, A.; Wang, J.L. Molecular level understanding of the chalcogen atom effect on chalcogen-based polymers through electrostatic potential, non-covalent interactions, excited state behaviour, and radial distribution function. *Polym. Chem.* **2022**, *13*, 5993–6001. [CrossRef]

21.   Mahmood, A.; Khan, S.U.D.; Rehman, F.U. Assessing the quantum mechanical level of theory for prediction of UV/Visible absorption spectra of some aminoazobenzene dyes. *J. Saudi Chem. Soc.* **2015**, *19*, 436–441. [CrossRef]

22.   Liu, J.Y.; Fang, W.J.; Wei, Z.D.; Qin, Z.; Jiang, Z.; Shangguan, W.F. Efficient photocatalytic hydrogen evolution on N-deficient g-C$_3$N$_4$ achieved by a molten salt post-treatment approach. *Appl. Catal. B-Environ.* **2018**, *238*, 465–470. [CrossRef]

23.   Yang, X.L.; Qian, F.F.; Zou, G.J.; Li, M.L.; Lu, J.R.; Li, Y.M.; Bao, M.T. Facile fabrication of acidified g-C$_3$N$_4$/g-C$_3$N$_4$ hybrids with enhanced photocatalysis performance under visible light irradiation. *Appl. Catal. B-Environ.* **2016**, *193*, 22–35. [CrossRef]

24.   Li, J.Q.; Qi, Y.; Mei, Y.Q.; Ma, S.C.; Li, Q.; Xin, B.F.; Yao, T.J.; Wu, J. Construction of phosphorus-doped carbon nitride/phosphorus and sulfur co-doped carbon nitride isotype heterojunction and their enhanced photoactivity. *J. Colloid. Interf. Sci.* **2020**, *566*, 495–504. [CrossRef] [PubMed]

25.   Li, K.; Chen, M.; Chen, L.; Zhao, S.; Xue, W.; Han, Z.; Han, Y. Synthesis of g-C$_3$N$_4$ Derived from Different Precursors for Photodegradation of Sulfamethazine under Visible Light. *Processes* **2023**, *11*, 528. [CrossRef]

26.   Dong, H.; Guo, X.T.; Yang, C.; Ouyang, Z.Z. Synthesis of g-C$_3$N$_4$ by different precursors under burning explosion effect and its photocatalytic degradation for tylosin. *Appl. Catal. B-Environ.* **2018**, *230*, 65–76. [CrossRef]

27.   Mou, Z.G.; Chen, T.; Tao, Y.; Gao, Y.; Sun, J.H.; Lei, W.I. Fabrication of g-C$_3$N$_4$/N,Fe co-doped CQDs composites: In situ decoration of g-C$_3$N$_4$ with N-CQDs and Fe and efficient visible-light photocatalytic degradation of tetracycline. *J. Phys. D Appl. Phys.* **2022**, *55*, 5. [CrossRef]

28.   Yang, C.; Xue, Z.; Qin, J.; Sawangphruk, M.; Zhang, X.; Liu, R. Heterogeneous structural defects to prompt charge shuttle in g-C$_3$N$_4$ plane for boosting visible-light photocatalytic activity. *Appl. Catal. B Environ.* **2019**, *259*, 118094. [CrossRef]

29.   Xia, X.; Xu, B.G.; Zhang, H.Y.; Ji, K.; Ji, X.S.; Wang, D.; Yang, P. NiCoP/g-C$_3$N$_4$ Schottky heterojunctions towards efficient photocatalytic NO oxidation. *J. Alloys Compd.* **2022**, *928*, 167207. [CrossRef]

30.   Yin, X.L.; Liu, J.; Jiang, W.J.; Zhang, X.; Hu, J.S.; Wan, L.J. Urchin-like Au@CdS/WO3 micro/nano heterostructure as a visible-light driven photocatalyst for efficient hydrogen generation. *Chem. Commun.* **2015**, *51*, 13842–13845. [CrossRef]

31.   Zhu, Y.F.; Liu, Y.F.; Ai, Q.; Gao, G.H.; Yuan, L.; Fang, Q.Y.; Tian, X.Y.; Zhang, X.; Egap, E.; Ajayan, P.M.; et al. In Situ Synthesis of Lead-Free Halide Perovskite-COF Nanocomposites as Photocatalysts for Photoinduced Polymerization in Both Organic and Aqueous Phases. *ACS Mater. Lett.* **2022**, *4*, 464–471. [CrossRef]

32.   Kang, J.; Jin, C.; Li, Z.; Wang, M.; Chen, Z.; Wang, Y. Dual Z-scheme MoS$_2$/g-C$_3$N$_4$/Bi$_{24}$O$_{31}$Cl$_{10}$ ternary heterojunction photocatalysts for enhanced visible-light photodegradation of antibiotic. *J. Alloys Compd.* **2020**, *825*, 153975. [CrossRef]

33.   Li, J.; Zhang, M.; Li, X.; Li, Q.; Yang, J. Effect of the calcination temperature on the visible light photocatalytic activity of direct contact Z-scheme g-C$_3$N$_4$-TiO$_2$ heterojunction. *Appl. Catal. B Environ.* **2017**, *212*, 106–114. [CrossRef]

34.   Zhang, J.; Fu, J.; Wang, Z.; Cheng, B.; Dai, K.; Ho, W. Direct Z-scheme porous g-C$_3$N$_4$/BiOI heterojunction for enhanced visible-light photocatalytic activity. *J. Alloys Compd.* **2018**, *766*, 841–850. [CrossRef]

35. Vattikuti, S.V.P.; Police, A.K.R.; Shim, J.; Byon, C. In situ fabrication of the Bi_2O_3-V_2O_5 hybrid embedded with graphitic carbon nitride nanosheets: Oxygen vacancies mediated enhanced visible-light-driven photocatalytic degradation of organic pollutants and hydrogen evolution. *Appl. Surf. Sci.* **2018**, *447*, 740–756. [CrossRef]

36. Du, F.Y.; Lai, Z.; Tang, H.Y.; Wang, H.Y.; Zhao, C.X. Construction of dual Z-scheme Bi_2WO_6/g-C_3N_4/black phosphorus quantum dots composites for effective bisphenol A degradation. *J. Environ. Sci.* **2023**, *124*, 617–629. [CrossRef]

37. Bi, J.; Wu, L.; Li, J.; Li, Z.; Wang, X.; Fu, X. Simple solvothermal routes to synthesize nanocrystalline Bi_2MoO_6 photocatalysts with different morphologies. *Acta Mater.* **2007**, *55*, 4699–4705. [CrossRef]

38. Yu, H.; Jiang, L.; Wang, H.; Huang, B.; Yuan, X.; Huang, J.; Zhang, J.; Zeng, G. Modulation of Bi_2MoO_6-based materials for photocatalytic water splitting and environmental application: A critical review. *Small* **2019**, *15*, 1901008. [CrossRef]

39. Di, G.; Zhu, Z.; Zhang, H.; Qiu, Y.; Yin, D.; Crittenden, J. Simultaneous sulfamethazine oxidation and bromate reduction by Pd-mediated Z-scheme Bi_2MoO_6/g-C_3N_4 photocatalysts: Synergetic mechanism and degradative pathway. *Chem. Eng. J.* **2020**, *401*, 126061. [CrossRef]

40. Opoku, F.; Govender, K.K.; van Sittert, C.G.C.E.; Govender, P.P. Insights into the photocatalytic mechanism of mediator-free direct Z-scheme g-C_3N_4/Bi_2MoO_6 (010) and g-C_3N_4/Bi_2WO_6 (010) heterostructures: A hybrid density functional theory study. *Appl. Surf. Sci.* **2018**, *427*, 487–498. [CrossRef]

41. Wu, H.; Meng, F.; Liu, X.; Yu, B. Carbon nanotubes as electronic mediators combined with Bi_2MoO_6 and g-C_3N_4 to form Z-scheme heterojunctions to enhance visible light photocatalysis. *Nanotechnology* **2021**, *33*, 115203. [CrossRef]

42. Zhong, K.D.; Feng, J.W.; Gao, H.B.; Zhang, Y.M.; Lai, K.R. Fabrication of $BiVO_4$@g-C_3N_4(100) heterojunction with enhanced photocatalytic visible-light-driven activity. *J. Solid State Chem.* **2019**, *274*, 142–151. [CrossRef]

43. Beketova, D.; Motola, M.; Sopha, H.; Michalicka, J.; Cicmancova, V.; Dvorak, F.; Hromadko, L.; Frumarova, B.; Stoica, M.; Macak, J.M. One-step decoration of TiO_2 nanotubes with Fe_3O_4 nanoparticles: Synthesis and photocatalytic and magnetic properties. *ACS Appl. Nano Mater.* **2020**, *3*, 1553–1563. [CrossRef]

44. Stefan, M.; Leostean, C.; Pana, O.; Toloman, D.; Popa, A.; Perhaita, I.; Senilă, M.; Marincas, O.; Barbu-Tudoran, L. Magnetic recoverable Fe_3O_4-TiO_2: Eu composite nanoparticles with enhanced photocatalytic activity. *Appl. Surf. Sci.* **2016**, *390*, 248–259. [CrossRef]

45. Elshypany, R.; Selim, H.; Zakaria, K.; Moustafa, A.H.; Sadeek, S.A.; Sharaa, S.; Raynaud, P.; Nada, A.A. Elaboration of Fe_3O_4/ZnO nanocomposite with highly performance photocatalytic activity for degradation methylene blue under visible light irradiation. *Environ. Technol. Innov.* **2021**, *23*, 101710. [CrossRef]

46. Blaney, L. *Magnetite (Fe_3O_4): Properties, Synthesis, and Applications*; Lehigh University Lehigh Preserve: Bethlehem, PA, USA, 2007; Volume 15, p. 5.

47. Hussain, S.; Alam, M.M.; Imran, M.; Ali, M.A.; Ahamad, T.; Haidyrah, A.S.; Alotaibi, S.M.R.; Shariq, M. A facile low-cost scheme for highly photoactive Fe_3O_4-MWCNTs nanocomposite material for degradation of methylene blue. *Alex. Eng. J.* **2022**, *61*, 9107–9117. [CrossRef]

48. Niu, P.; Zhang, L.; Liu, G.; Cheng, H.M. Graphene-like carbon nitride nanosheets for improved photocatalytic activities. *Adv. Funct. Mater.* **2012**, *22*, 4763–4770. [CrossRef]

49. Jiang, M.; Zou, Y.; Xu, F.; Sun, L.; Hu, Z.; Yu, S.; Zhang, J.; Xiang, C. Synthesis of g-C_3N_4/Fe_3O_4/MoS_2 composites for efficient hydrogen evolution reaction. *J. Alloys Compd.* **2022**, *906*, 164265. [CrossRef]

50. Li, S.; Shen, X.; Liu, J.; Zhang, L. Synthesis of Ta_3N_5/Bi_2 MoO_6 core–shell fiber-shaped heterojunctions as efficient and easily recyclable photocatalysts. *Environ. Sci. Nano* **2017**, *4*, 1155–1167. [CrossRef]

51. Irianti, F.; Sutanto, H.; Priyono, P.; Wibowo, A.; Syahida, A.; Alkian, I. Characterization structure of Fe_3O_4@ PEG-4000 nanoparticles synthesized by co-precipitation method. *J. Phys. Conf. Ser.* **1943**, *1943*, 012014. [CrossRef]

52. Zhang, H.; Zhao, L.X.; Geng, F.L.; Guo, L.H.; Wan, B.; Yang, Y. Carbon dots decorated graphitic carbon nitride as an efficient metal-free photocatalyst for phenol degradation. *Appl. Catal. B-Environ.* **2016**, *180*, 656–662. [CrossRef]

53. Bavani, T.; Madhavan, J.; Preeyanghaa, M.; Neppolian, B.; Murugesan, S. Construction of direct Z-scheme g-C_3N_4/BiYWO6 heterojunction photocatalyst with enhanced visible light activity towards the degradation of methylene blue. *Environ. Sci. Pollut. Res.* **2022**, *30*, 10179–10190. [CrossRef]

54. Preeyanghaa, M.; Dhileepan, M.D.; Madhavan, J.; Neppolian, B. Revealing the charge transfer mechanism in magnetically recyclable ternary g-C_3N_4/BiOBr/Fe_3O_4 nanocomposite for efficient photocatalytic degradation of tetracycline antibiotics. *Chemosphere* **2022**, *303*, 135070. [CrossRef] [PubMed]

55. Iordanova, R.; Dimitriev, Y.; Dimitrov, V.; Kassabov, S.; Klissurski, D. Glass formation and structure in the system MoO3–Bi2O3–Fe2O3. *J. Non-Cryst. Solids* **1998**, *231*, 227–233. [CrossRef]

56. Fialips, C.-I.; Huo, D.; Yan, L.; Wu, J.; Stucki, J.W. Effect of Fe oxidation state on the IR spectra of Garfield nontronite. *Am. Mineral.* **2002**, *87*, 630–641. [CrossRef]

57. Yang, N.; Li, G.; Wang, W.; Yang, X.; Zhang, W. Photophysical and enhanced daylight photocatalytic properties of N-doped TiO_2/g-C_3N_4 composites. *J. Phys. Chem. Solids* **2011**, *72*, 1319–1324. [CrossRef]

58. Zhang, G.; Wu, Z.; Liu, H.; Ji, Q.; Qu, J.; Li, J. Photoactuation healing of α-FeOOH@ g-C_3N_4 catalyst for efficient and stable activation of persulfate. *Small* **2017**, *13*, 1702225. [CrossRef] [PubMed]

59. Dong, F.; Zhao, Z.; Xiong, T.; Ni, Z.; Zhang, W.; Sun, Y.; Ho, W.-K. In situ construction of g-C_3N_4/g-C_3N_4 metal-free heterojunction for enhanced visible-light photocatalysis. *ACS Appl. Mater. Inter.* **2013**, *5*, 11392–11401. [CrossRef] [PubMed]

60. Cui, Z.; Yang, H.; Zhao, X. Enhanced photocatalytic performance of g-C$_3$N$_4$/Bi$_4$Ti$_3$O$_{12}$ heterojunction nanocomposites. *Mater. Sci. Eng. B* **2018**, *229*, 160–172. [CrossRef]
61. Habibi-Yangjeh, A.; Mousavi, M.; Nakata, K. Boosting visible-light photocatalytic performance of g-C$_3$N$_4$/Fe$_3$O$_4$ anchored with CoMoO$_4$ nanoparticles: Novel magnetically recoverable photocatalysts. *J. Photochem. Photobiol. A Chem.* **2019**, *368*, 120–136. [CrossRef]
62. Amer, M.; Matsuda, A.; Kawamura, G.; El-Shater, R.; Meaz, T.; Fakhry, F. Characterization and structural and magnetic studies of as-synthesized Fe^{2+} CrxFe $_{(2-x)}$ O$_4$ nanoparticles. *J. Magn. Magn. Mater.* **2017**, *439*, 373–383. [CrossRef]
63. Tang, J.; Myers, M.; Bosnick, K.A.; Brus, L.E. Magnetite Fe$_3$O$_4$ nanocrystals: Spectroscopic observation of aqueous oxidation kinetics. *J. Phys. Chem. B* **2003**, *107*, 7501–7506. [CrossRef]